Bimetallic Synergy in CoPd Nanocatalysts for CO Oxidation

Cheng Hao Wu[1,2], Chang Liu[3], Dong Su[4], Huolin Xin[4], Haitao Fang[2,5], Baran Eren[5], Sen Zhang[3,*], Christopher B. Murray[6,*], Miquel B. Salmeron[2,7,*]

[1] Department of Chemistry, University of California, Berkeley, Berkeley CA, USA
[2] Materials Science Division, Lawrence Berkeley National Laboratory, Berkeley CA, USA
[3] Department of Chemistry, University of Virginia, Charlottesville, Virginia 22904, USA
[4] Center for Functional Nanomaterials, Brookhaven National Laboratory, Upton, New York 11973, USA
[5] School of Materials Science and Engineering, Harbin Institute of Technology, Harbin, Heilongjiang 150001, China
[6] Department of Chemistry, University of Pennsylvania, Philadelphia, Pennsylvania 19104, USA
[7] Department of Materials Science and Engineering, University of California, Berkeley, Berkeley CA, USA

*Corresponding Authors:
Email for S.Z.: sz3t@virginia.edu
Email for C.B.M.: cbmurray@sas.upenn.edu
Email for M.B.S.: mbsalmeron@lbl.gov

Abstract

Bimetallic and multi-component catalysts often exhibit superior activity and selectivity compared with their single-component counterparts. To investigate the origin of the composition dependence observed in the catalytic activities of CoPd bimetallic catalysts, the compositional and structural evolution of monodisperse CoPd alloy nanoparticles (NPs) were followed under catalytic CO oxidation conditions using ambient pressure X-ray spectroscopy (AP-XPS) and transmission electron microscopy (TEM). It was found that the catalysis process induced a reconstruction of the catalysts, leaving CoO_x on the NP surface. The synergy between Pd and CoO_x coexisting on the surface promotes the catalytic activity of the bimetallic catalysts. Such synergistic effects can be optimized by tuning the Co/Pd ratios in the NP synthesis and reach a maximum at compositions near $Co_{0.26}Pd_{0.74}$, which exhibits the lowest temperature for complete CO conversion. Our combined AP-XPS and TEM studies provide a direct observation of the bimetallic NPs surface evolution under catalytic conditions and its correlation to catalytic properties.

Catalytic CO oxidation has been extensively studied as a model reaction,[1–5] because of its important industrial applications in automotive exhaust treatment,[6,7] and in fuel purification (removal of trace amount of CO from hydrogen fuels) for proton exchange membrane fuel cells.[8,9] Mechanistic studies on such model reactions and the catalysts that promote them can advance the development of catalysts for many relevant catalytic processes such as water-gas shift reaction and methanol oxidation.[5]

One strategy that has proven successful to produce efficient heterogeneous catalysts for CO oxidation is to create a synergistic interface between precious metals (PM; e. g. Pt, Au, and Pd) and active metal oxides (AMO; e.g., TiO_2, CeO_2, Co_3O_4, and NiO)[10–15] that provides "active" lattice oxygen to oxidize the CO adsorbed on the adjacent PM atoms. The lattice oxygen vacancies created in this process can bind O_2 and be created later again to restart the catalytic cycle. Such PM/AMO interface can be build-up by loading PM nanoparticles (NPs) onto AMO,[16,17] or by alloying PM NPs with other metals as reported in the examples of FePt,[18] FeNi,[19] NiPd,[20] and CuAu.[21] The later approach is particularly appealing, as it potentially allows the interfacial effect to be realized at the atomic level on the entire NP surface. Recent advances in the colloidal synthesis of monodisperse alloy NPs have enabled us to tune the bimetallic composition on NPs with well-defined sizes and shapes.[22–24] However, bimetallic alloy NPs are prone to changes during activation or reaction. These changes include reconstructions, segregation, and oxidative/reductive evolution,[20,25–27] all of which can significantly impact the activity and durability of the catalysts. A more precise understanding of these reaction-induced modifications is essential to elucidate reaction mechanism and optimize the bimetallic NP catalyst' reactivity and selectivity for CO oxidation.

Recent advances in *in situ/operando* surface characterization[28–32] have made it possible to study catalyst surfaces and their interaction with gas-phase reactants under reaction conditions. One example is the development of ambient-pressure x-ray photoelectron spectroscopy (AP-XPS), which makes this traditionally vacuum-requiring surface analysis tool operational under reactant gases up to Torr pressures.[28,33] Herein, we combined an *in situ* AP-XPS investigation of monodisperse CoPd NPs under CO oxidation conditions with *in situ* and *ex situ* (scanning) transmission electron microscopy [(S)TEM] and electron energy loss spectroscopy (EELS), as well as *ex situ* x-ray absorption spectroscopy. This integrated study reveals the surface/structure evolution and bimetallic synergy of NP catalysts in action. We observed that the atomic surface composition of the CoPd alloy NPs transformed during the oxidation/reduction pre-treatments. At 200 and 300°C, exposure to CO drives Pd atoms to migrate to the surface, whereas O_2 exposure does the opposite. Such reversible reactant-driven surface segregation however, becomes less prominent with increasing Co content and is eventually negligible in the case of $Co_{0.52}Pd_{0.48}$ NPs, where the NPs with highest Co content the surface becomes completely covered by CoO_x as corroborated by STEM-EELS mapping. The observed segregation behavior in CoPd NPs suggested that Pd and CoO_x coexist on the catalyst surface both exposed to the reactant gases, at least for NPs Co content below 50%. The Pd/CoO_x coexistence contributes to the promotion of the CO oxidation kinetics. This mechanism explains the trend of the catalytic properties of five NP catalysts of different compositions from pure Pd to $Co_{0.52}Pd_{0.49}$, among which the $Co_{0.26}Pd_{0.74}$ shows the lowest temperature for complete conversion of CO to CO_2. This work highlights the benefits of using well-

4

defined NPs as model catalysts together with *in situ* characterization techniques in understanding the bimetallic synergy under catalytic conditions.

Synthesis of CoPd NPs and their catalytic performance in CO oxidation

CoPd NPs were synthesized by the co-reduction of palladium bromide ($PdBr_2$) and cobalt acetylacetonate [$Co(acac)_2$] in a solution of oleylamine (OAm) in the presence of tributylphosphine (TBP), as modified from a previously reported method.[34] OAm was used as both a solvent and a reducing agent to generate metallic alloy NPs. In contrast to previous methods in which trioctylphosphine (TOP) functions as a surfactant and leads to larger NPs, we used a less bulky phosphine capping agent TBP, to obtain smaller NPs with higher surface area, because the less bulky TBP imposes a weaker steric hindrance than TOP, allowing more nuclei to form in the nucleation process and thus leaving fewer atoms for NP growth.[35] As shown in the representative high-angle annular dark field (HAADF) and bright field TEM images in Fig. 1A and S1B, $Co_{0.26}Pd_{0.74}$ NPs synthesized with TBP surfactant exhibit an average size of 4.5 ± 0.2 nm, half the size of $Co_{0.26}Pd_{0.74}$ obtained with TOP (9.0 ± 0.5 nm, Fig. S1F). The composition of bimetallic alloy NPs can be readily tuned by changing the molar ratio of $PdBr_2$/$Co(acac)_2$ in the synthesis. Fig. S1 shows TEM images of CoPd NPs with various Co content, including $Co_{0.10}Pd_{0.90}$, $Co_{0.26}Pd_{0.74}$, $Co_{0.38}Pd_{0.62}$, and $Co_{0.52}Pd_{0.48}$, as measured by inductively coupled plasma - optical emission spectroscopy (ICP-OES). Without any post size-selection process, all NP samples are highly uniform with an average size of 4.5 ± 0.3 nm. Within each NP, Co and Pd are homogeneously distributed, forming a solid solution structure, as confirmed by the two-dimensional elemental mapping via aberration-corrected STEM (Fig. 1B-D). For a control

5

experiment 4.5nm Pd NPs were synthesized using the similar approach (Fig. S1E). All the as-synthesized CoPd alloy NPs exhibit glass-like fcc structures and weaker peaks in XRD patterns (Fig. S2) compared to Pd NPs, consistent with other NPs synthesized using phosphine stabilizers.[36]

Before catalytic performance test, the as-synthesized CoPd and Pd NPs were dispersed onto alumina support and then pre-treated to remove the surface ligands, as described in the Methods. Alumina was chosen as the catalyst support in this study because of its relative inertness compared with titania and ceria, which allowed us to focus exclusively on the catalytic nature of the alloy NPs.[17] In addition, the high-surface-area alumina support can protect the NPs from sintering during annealing, as shown in TEM images of catalyst before and after surface activation (Fig. S3).

Fig. 2A shows the light-off curves of CoPd and Pd NP catalysts for CO oxidation under identical testing conditions (1.0% CO, 4.0% O_2 in He). The incorporation of Co clearly helps lower the temperature needed to completely oxidize CO in the gas mixture for all bimetallic NP catalysts except the NPs with the highest Co content ($Co_{0.52}Pd_{0.48}$). Among all the five NPs, $Co_{0.26}Pd_{0.74}$ NPs can achieve complete CO conversion at the lowest temperature, around 110°C, much lower than Pd NPs (~180 °C).[17] Based on the kinetics measurements (Fig. 2B), the apparent activation energy (E_a) of $Co_{0.26}Pd_{0.74}$ calculated from the corresponding Arrhenius-type plot is 41.6 ± 3.7 KJ mol^{-1}, lower than 61.5 ± 5.9 KJ mol^{-1} of Pd. The catalysis test suggested that the bimetallic composition is favorable for enhanced CO oxidation kinetics and, more importantly, Co content is crucial to optimize this enhancement.

Surface evolution of Pd and Co_xPd_{1-x} NPs after catalyst pretreatments

Untreated NPs showed an intense C$1s$ peak with weak Pd$3d$ or Co$3p$ signals because of the thick layers of organic ligands surrounding each NP. Before exposing the NPs to the reactant gases, the NPs were submitted to an oxidation/reduction pretreatment in the AP-XPS chamber as described in the Methods. After the pretreatment some residual carbon was still present on the surface of NPs with higher Co content (Fig. S4), a result of the high solubility of carbon in Co/CoO$_x$.[37] Pd$3d$ spectra collected during the pretreatment processes showed that on the alloy NP surface, Pd was partially oxidized and reduced during oxidation/reduction cycles as expected, but Co remained oxidized, with little change noticeable in the Co$3p$ XPS region.

For pure Pd NPs, the Pd was almost fully oxidized to PdO (binding energy or BE at 336.0eV) after oxidation and fully reduced to metallic Pd (BE at 335.2eV) after reduction in H$_2$,[38,39] as shown in Fig. S5. The corresponding Pd$3d$ spectra were used as reference spectra to determine the line shapes and fitting parameters in the subsequent analysis of all other Pd$3d$ spectra (more details in the supplementary information or SM).

Surface evolution of Pd and CoPd NPs under catalytic conditions

To understand the interactions between the NPs catalyst and reactants, the pre-treated CoPd NPs were first exposed to 100mTorr of O$_2$ or 100mTorr of CO separately at different temperatures. At 300°C, CoPd NPs were exposed to 100mTorr of CO and O$_2$ mixture with different CO/O$_2$ ratios (1:4 or 4:1). Pd$3d$, Co$3p$/Pd$4p$, and C$1s$ XPS spectra were monitored during these processes, with an incident photon energy of 500eV. The photoelectrons excited from Pd$3d$ orbitals with 500eV x-ray photons have kinetic energies are around 160eV, which corresponds to a probing depth of approximately 0.5nm.

When pure Pd NPs were exposed to 100mTorr of O_2 or CO at room temperature (RT), the Pd3d

spectra exhibited no obvious change (Fig. 3A) except for a slight decrease (~13%) in peak intensity

under CO exposure. Such decrease is likely due to the presence of high coverage of adsorbed CO

molecules on the surfaces, which reduces the intensity of Pd3d signals.[40] The widths of the Pd $3d_{5/2}$

peaks under both O_2 and CO at RT are slightly larger than that of metallic Pd $3d_{5/2}$ peak (collected after

reduction in H_2 as shown in Fig. S5A) and an extra component at 0.6-0.7eV higher BE than the metallic

Pd peak was needed to fit the overall line shape. The chemical origin of this extra component is different

under CO and O_2: When exposed to CO, the BE of CO-coordinated surface Pd atoms could blue-shift

about 0.6eV compared to metallic Pd atoms,[38] whereas in O_2 Pd atoms coordinated by two O atoms (a

surface sub-oxide) is responsible for the extra component.[38,39] C1s spectra under CO shown in Fig. 3B

show three peaks at ~284, ~285.8, and ~291eV, corresponding to residual surface carbon species,

adsorbed CO, and gas-phase CO, respectively. The last two peaks disappeared upon exposure to O_2,

while the residual surface carbon decreased substantially.

At 200°C and 300°C, the Pd3d spectra exhibited a more prominent shoulder at higher BE than

metallic Pd when exposed to O_2. Peak fitting (Fig. S5) revealed the existence of substantial bulk PdO

with 4-fold O-coordination, with a peak centered at ~336.0 eV.[38,39] A weak residual component above

337 eV in the $3d_{5/2}$ region is likely related to the energy-loss feature of PdO [41,42] and/or a more oxidized

Pd species. Under CO, adsorbed CO peaks were discernible in C1s spectra at both 200°C and 300°C;

and the Pd NP surface was more reduced. No bulk PdO was present at either temperature but a small

component at ~335.7eV is needed to fit the overall line shape (Fig. S5). The width of this extra

component (~1eV) is consistently smaller than that of surface sub-oxide (~1.5eV), suggesting a different origin for this component. Previous studies on CO adsorption[38] and decomposition[43] on Pd surfaces hinted that both CO-coordinated Pd (Pd-CO) and surface carbide PdC_x could be responsible for the appearance of the peak at 335.7eV, but the absence of carbide peak (~283eV) in C$1s$ spectrum rules out the presence of carbide.

When exposed to O_2 rich and CO rich mixtures of CO and O_2 at 300°C, the Pd$3d$ spectra became indistinguishable, with the peak fitting revealing that surface Pd atoms remained mostly metallic, with small contribution (~3%) of bulk oxide and ~30% surface sub-oxide. The evolution of the Pd species is summarized in Fig. 4A. A very weak CO gas-phase peak and an adsorbed CO peak in the C$1s$ spectra (Fig. 3B, top) indicated fast turn-over of the reactants under such conditions. The existence of surface oxides with no CO adsorption under such conditions is in line with theoretically predicted surface phase diagram of Pd (100) under CO/O_2 mixtures.[44]

For NP with low Co content, i.e. $Co_{0.10}Pd_{0.90}$ and $Co_{0.26}Pd_{0.74}$, there was no obvious change in Pd$3d$ spectra at RT except for a small drop in intensity (~11% and ~5% respectively) under CO, as shown in Fig. S6A and 3C. At 200 °C, a shoulder emerged under O_2 on the high BE side of the Pd $3d_{5/2}$ peak, indicating oxidation of surface Pd atoms. At 300 °C the intensity of Pd$3d$ peaks was larger under CO than under O_2 and such intensity variation was reversible, indicating reversible surface segregation of Pd depending on the gas environment. Such reversibility was corroborated by Co/Pd ratios estimated from the XPS peaks in the Co$3p$/Pd$4p$ region (Fig. S8). The surface segregation behavior of the alloy catalysts, which was enhanced by the increased diffusion rate at elevated temperatures, can be

rationalized by the relatively lower surface energies of Pd relative to CoO_x under CO, and CoO_x relative to Pd/PdO_x in O_2. Similar segregation behavior has also been observed on several other bimetallic systems including PdRh and PtRh NPs.[25,26] Under the mixtures of CO and O_2 (both 1:4 and 4:1 ratios) at 300 °C, neither the overall Pd$3d$ intensities nor the surface Pd composition exhibited prominent difference.

Peak deconvolution of the Pd$3d$ spectra revealed more details of the chemical state of the surface Pd atoms. The evolution of all relevant surface Pd species under each condition is summarized in Fig. 4B and C. Under the conditions of our experiments, the percentage of bulk-like PdO appeared to vary by a larger extent when switching between CO and O_2 at different temperatures, but the percentage of surface sub-oxide/Pd-CO remained (but difficult to distinguish) relatively unchanged (~20% for $Co_{0.10}Pd_{0.90}$, and ~30% for $Co_{0.26}Pd_{0.74}$). Under the different CO/O_2 mixtures, the Co/Pd ratios and the chemical state of Pd were similar to those under O_2, as shown in Fig. 4B, C, and S8. Meanwhile, the Co$3p$ spectra showed that Co stayed oxidized under all the conditions.

Given the fact that pure Pd NPs can be fully reduced in H_2 (at 150°C) as shown in Fig. 4A and S5, the residual Pd sub-oxide observed in $Co_{0.10}Pd_{0.90}$ is possibly a consequence of CoO_x formation and its interface with surrounding Pd atoms. Unfortunately, the adsorbed CO peak was overwhelmed by the intense carbon residuals peak because of high solubility of carbon in Co/CoO_x.[37] Moreover, our previous study on Co foils demonstrated accumulation of CoC_x species under CO.[45] As a result, we cannot completely rule out the interaction between carbide-like carbon atoms with Pd atoms, especially at the interface between Pd and Co/CoO_x. Although surface Pd sub-oxide (including Pd atoms in contact with

10

CoO_x), CO-coordinated Pd (Pd-CO), and PdC_x may coexist on the surface, their Pd$3d$ peaks are very close and thus difficult to distinguish in the fitting process. For that reason they were represented by one single component in the peak deconvolution of all the Pd$3d$ spectra of alloy NPs.

For samples with relatively high Co content, i.e., $Co_{0.38}Pd_{0.22}$ and $Co_{0.52}Pd_{0.48}$, the signal-to-noise ratios of the Pd$3d$ spectra (Fig. S6B and 3D) became noticeably worse, while Co$3p$ signal was substantially more intense (Fig. S7B) in the Co$3p$/Pd$4p$ region. Unlike the cases of $Co_{0.10}Pd_{0.90}$ and $Co_{0.26}Pd_{0.74}$, under all the tested conditions, neither the intensity nor the line shape of the Pd$3d$ and Co$3p$/Pd$4p$ peak exhibited large variations. Although the noisier Pd$3d$ and Pd$4p$ signals potentially brought larger errors in the fitting process, tentative fitting results on $Co_{0.38}Pd_{0.22}$ also suggested smaller variations in the surface compositions (both Co/Pd ratios and percentages of Pd species) under all the tested conditions, as shown in Fig. 4D and S8. Co$2p$ XPS spectra would be more useful to further analyze the chemical states of the surface Co species. Unfortunately the photon flux and energy resolution above 750eV at the beam line used here prevented us from acquiring meaningful Co$2p$ spectra, especially under *in situ* conditions.

In situ EELS and *ex situ* XAS characterization

In order to take a close look at the chemical states of Co in the alloy NPs, we carried out STEM/EELS measurements on $Co_xPd_{(1-x)}$ NPs under conditions similar to the AP-XPS experiments using an environmental TEM (ETEM). Co$2p$ EELS spectra collected after heating in CO/O_2 mixtures for 40min at 200°C, exhibited an L_3/L_2 ratio of ~3.8, lower than that under reducing environments (5.0~5.2 after H_2 pretreatment or under CO only; shown in Fig. S9). The L_3/L_2 ratio in the EELS spectra

is reported to be an indicator of the oxidation states of 3d transition metals.[46,47] The measured L_3/L_2 ratios suggested mostly Co^{2+} under reducing environment in H_2 or CO and a mixture of Co^{2+}/Co^{3+} in the mixture of CO/O_2. *Ex situ* x-ray absorption spectroscopy (XAS) measurements on the post-reaction NPs also suggested complete oxidation of Co. As illustrated in Fig. S10, the bulk-sensitive partial fluorescence yield (PFY) XAS spectra of all four alloy NPs shows dominating Co(III) characteristics, whereas the surface sensitive total electron yield (TEY) XAS spectra showed substantial Co(II) species on the surface.

Composition-dependent bimetallic synergy

The aforementioned activity test clearly showed a clear correlation between the composition of Co_xPd_{1-x} NPs and their catalytic activity for CO oxidation. Based on the surface evolution observed in both spectroscopic and microscopic characterizations, we propose a mechanism for the synergy of bimetallic PdCo NPs as shown in Fig. 5, which illustrates the composition-dependent structure change of PdCo NPs under CO oxidation conditions.

Pd and Co are uniformly distributed in the as-synthesized alloy NPs, as evidenced by STEM-EELS elemental mapping in Fig. 1 and S1. After the pre-treatment to remove surfactants, Co is segregated to the surface of NPs as an oxide. Heating in H_2 at 150°C partially reduces Pd on the surface but the temperature is not sufficient to reduce the CoO_x to Co metal.[45] It is clear that a large Co content in the NPs would produce a surface CoO_x layer that would completely cover the Pd core, as shown by *ex-situ* STEM image and EELS mapping (Figure S11) of pre-treated $Co_{0.52}Pd_{0.48}$ NPs. Low Co content on the other hand would produce a partial coverage on the surface, exposing metallic Pd and creating a

substantial amount of boundaries and interfaces between Pd and CoO_x, which are prime candidates for sites where the CO oxidation is enhanced. For the 4.5 nm NPs used here, the composition that would produce one complete monolayer of CoO_x, if completely segregated to the surface, can be estimated as being around 20% (see supporting information), not far from the experimental composition of $Co_{0.26}Pd_{0.74}$ that produces the best catalyst.

The strong adsorption of CO on metallic Pd, together with the high oxygen affinity of Co drives the surface composition changes with segregation of Co under O_2 and Pd under CO. In addition to the increased island perimeter at low Co content where oxygen atoms from CoO_x can be passed on to a CO molecule on neighboring Pd atoms to form a CO_2 molecule, CO may also react with O atoms on the Pd-supported CoO_x monolayer, producing O-vacancies and thus activating Co for CO adsorption and reaction with lattice O. These two effects are maximized at CoO_x coverages near or below one monolayer, which is expected to occur near the optimal composition determined in our catalytic CO oxidation studies. Unfortunately, imaging a monolayer thin CoO_x shell on a 4.5nm NP surface is very challenging in STEM and we were not able to obtain conclusive images of monolayer thin shells, except for small CoO_x clusters occasionally spotted on the NP surface, as shown in the STEM image and EELS mapping in Figure S12. However, larger particles with the same composition produce thicker shells, easier to observe in STEM, as shown for the 10nm $Co_{0.24}Pd_{0.76}$ NPs in Fig. 6, where a thin Co shell covering the Pd core is visible, thus corroborating the Co segregation behavior deduced from the AP-XPS results.

13

At higher Co content the segregated CoO_x species eventually form a thick continuous shell covering the entire Pd core, as clearly demonstrated in the case of $Co_{0.52}Pd_{0.48}$ (Figure S11). The deeper buried Pd core is thus isolated from the gas reactants, and the CoO_x shell is solely responsible for the CO oxidation, which proves to be a worse catalyst for CO oxidation than pure Pd. One can imagine that a higher reduction temperature may help to further reduce CoO_x back to its metallic phase, resulting in the formation of a PdCo alloy again. With coexistence of both elements on the surface, the synergetic effect should become prominent again. Indeed, a control experiment in which the $Co_{0.52}Pd_{0.48}$ NPs were treated in H_2 (5.0% in He) at 400 °C supports this hypothesis. As shown in Fig. 7, the resulting alloy NPs initially showed much enhanced catalytic activity as the reduced Co alloying into the NP restored the optimal ratio of CoO_x-Pd and boundary or interface sites, but became rapidly deactivated above 150 °C, because of re-segregation and oxidation of the Co on the surface.

The proposed mechanism for synergetic effect of CoPd NPs explains why an optimal Co composition exists for the catalytic CO oxidation reaction, where the Co segregation and oxidation on the surface play an important role. Similar segregation behaviors were also observed on several surface alloys such as PdSn and PtSn, where Sn segregates to the surface under oxidative conditions and forms thin layers of SnO_x that wet the entire alloy surface.[48,49] Moreover, these thin oxide overlayers were found to be substantially less thermally stable than their bulk counterpart,[48,49] which makes them more likely to participate in the catalytic cycles involving oxygen. It is possible that such bimetallic synergy originated from selective segregation is responsible for many examples of composition-dependent catalytic activity reported in the literature.

14

Conclusion

In conclusion, we used AP-XPS and other complementary characterization techniques to investigate the surface evolution of a series of PdCo alloy NPs under CO oxidation reactions and revealed the origin of the composition dependence of their catalytic activity. It was found that under reaction conditions Co segregated to the surface as an oxide after pre-treatment. Exposure to CO at elevated temperatures drove more Pd to migrate to the surface whereas O_2 exposure did the opposite. The variation in surface composition under CO or O_2 became less prominent with increasing Co content because of increasing CoO_x coverage. The correlation between catalytic performance and surface composition indicates that coexisting Pd and CoO_x on the surface provides the sites that are responsible for promoting CO oxidation kinetics. We anticipate such composition-dependent surface segregation behavior and synergistic effect play essential roles in many other bimetallic catalyst systems. Our study illustrated that the use of advanced *in situ* characterization techniques facilitates the fundamental understanding of relevant surface phenomena and provides meaningful guidance towards the design and optimization of bimetallic and multi-component catalysts.

Methods

Chemicals and materials. Oleylamine (OAm, >70%), tributylphosphine (TBP, 97%), trioctylphosphine (TOP, 97%), palladium bromide ($PdBr_2$, 99%), palladium aceylacetonate ($Pd(acac)_2$, 99%), and cobalt acetylacetonate ($Co(acac)_2$, 97%) were all purchased from Sigma Aldrich and used without further purification. Hexane, isopropanol and acetone were all purchased from Fisher Scientific and used

without further purification. Alumina was purchased from Sasol (TH100/150) and calcined at 900°C for 24 hours for further usage.

Synthesis of Pd and CoPd alloy NPs. In a typical synthesis of $Co_{0.26}Pd_{0.74}$ NPs, 52mg of $Co(acac)_2$ and 81mg of $PdBr_2$ was mixed with 18mL of OAm and 0.25mL of TBP under stirring. The mixture was heated to 85°C for 1 hour under vacuum to generate a brown transparent solution with the impurities and moistures removed, and then protected with N_2. The solution was further heated to 260°C at a rate of 5°C /min and kept at this temperature for 2 hours before cooling to room temperature. The NPs were separated by adding 50mL of isopropanol into the mixture, followed by centrifugation (8500rpm, 8min). The NPs were further purified via cycles of dispersing (adding hexane), precipitation (adding isopropanol), and centrifugation, and then stored in hexane under the ambient condition.

Using the same conditions, simply varying the amounts of Co precursor to 26mg, 78mg and 104mg of $Co(acac)_2$ can yield $Co_{0.10}Pd_{0.90}$, $Co_{0.38}Pd_{0.62}$, and $Co_{0.52}Pd_{0.48}$, respectively. To obtain Pd NPs, 90mg of $Pd(acac)_2$ instead of $PdBr_2$ were used in the above synthetic procedure without adding $Co(acac)_2$ precursor.

Catalyst loading, activation and catalysis evaluation. Appropriate amount of NPs dissolved in hexane was added to a dispersion of Al_2O_3 in 15mL of hexane (to obtain a final metal loading of 0.5 wt.% verified by ICP-OES), and was stirred for 3 hours to allow NPs to be completely absorbed onto Al_2O_3. The NPs-Al_2O_3 composite was collected by centrifugation and washed with acetone. The solid powder was dried under vacuum overnight and then annealed in air at 300°C for 3 hours to completely remove the organic surfactants.

16

The catalyst was sieved below 150μm of grain size, and then put into the reactor quartz tube (inner diameter: 3.8mm) and immobilized by two layers of quartz wool for preventing displacement of the catalyst powder. Before CO oxidation catalysis testing, the catalyst was activated through a mild reduction at 150°C for 30mins in the presence of H_2 (5% H_2 in the He). CO oxidation was performed under an oxidative gas condition at atmospheric pressure. We used a mixed gas of CO, O_2 and He (1.0% CO, 4.0% O_2) with a constant flow rate of 30 mL min^{-1} and a gas hourly space velocity (GHSV) of 60000 mL g^{-1} h^{-1}. For light-off curve experiment, the reactant mixture was heated up to a desired temperature with a ramping rate of 3 °C min^{-1}. The composition of the effluent gases was monitored on-line using a Gas Chromatograph (GC) (Buck Scientific 910) equipped with a thermal conductivity detector (TCD), using He as the carrier gas.

AP-XPS. Measurements were carried out at the beamline 9.3.2 of the Advanced Light Source at Lawrence Berkeley National Laboratory. Before the experiment session started, the measurement chamber was baked at 120°C for more than 24 hours and the base pressure in the measurement chamber reached low 10^{-9} Torr. Prior to introduction of CO into the measurement chamber, the CO gas (99.99% purity) was passed through a hot trap of copper beads at 250°C, to remove any carbonyl contaminants. Similarly, ultra-pure H_2 gas (99.999% purity) passed through a liquid nitrogen trap to minimize residual water impurities by freezing.

Because the insulating nature of alumina support we used in the catalytic performance test can induce severe charging effects during XPS measurements, instead of being loaded on alumina support,

the NPs were drop-casted on a piece of silicon substrate for AP-XPS measurements. The native oxide layer on the silicon surface served as a substitute of inert oxide support for the catalysts.

Because the limitation on pressures in AP-XPS system, the pre-treatment procedures of the NPs sample were modified accordingly. The modified pre-treatment procedure involves a few cycles of oxidation/reduction, until the carbon composition in the XPS spectra stays mostly unchanged between two consecutive reduction cycles. Each oxidation step was performed under 500mTorr O_2 at 300°C for 20 minutes, and each reduction step under 200mTorr H_2 at 150°C for 20 minutes. C*1s* XPS spectra were continuously monitored during the pretreatment. After completing each oxidation/ reduction step, XPS spectra in Pd*3d*, Co*3p*/Pd*4p*, and C*1s* regions also were collected.

The procedure of spectra analysis, including energy calibration and peak deconvolution, was described in detail in the supporting information.

S/TEM and EELS characterization. High resolution ex-situ STEM analyses on CoPd NPs were carried out using a Hitachi HD2700C (200kV) with a probe aberration-corrector, in the Center for Functional Nanomaterials at Brookhaven National Lab. The EELS spectra and mapping were collected using a high resolution Gatan-Enfina ER with a probe size of 1.3Å, typical probe current of 80-100pA, a dwell time of 0.07s at binning of 100. A power law function was used for EELS background subtraction. For as-synthesized Co_xPd_{1-x} alloy NPs, samples were prepared by depositing a single drop of diluted NP dispersion in hexane on an ultrathin carbon (<3nm)/holey support film coated copper grid. For pretreated $Co_{0.52}Pd_{0.48}$ NPs, $Co_{0.52}Pd_{0.48}$ were loaded onto carbon (Vulcan-72, Fuel Cell Stores) with a NPs/Carbon weight ratio of 1:1 and then annealed in air at 300 °C for 3 hours to completely remove the

organic surfactants. The pretreated $Co_{0.52}Pd_{0.48}$ NPs supported on carbon were dispersed in acetone and transferred on an ultrathin carbon (<3nm)/holey support film coated copper grid for STEM characterization. We use carbon to replace Al_2O_3 here because the latter one is subject to charge accumulation under high energy electron beam and makes 2D EELS mapping insurmountably challenging.

Environmental S/TEM study of CoPd NPs were performed in an FEI Environmental Titan S/TEM operated at 300 keV. This instrument is equipped with a differential pumping system, a Schottky field-emission gun, an objective-lens aberration corrector, a Gatan Tredium electron energy loss spectrometer, and a gas manifold that can mix and flow four different gas streams. Under heating condition, CO is prone to decompose under the high-energy electron beam and causes carbon contamination to the catalysts. To avoid that, we collected in-situ EELS spectra in the TEM mode to spread the dose.

Other Structure and composition characterizations. X-ray powder diffraction (XRD) patterns were obtained on a Rigaku Smartlab diffractometer with Cu Kα radiation (λ=1.5418Å). Quantitative elemental analyses for the composition of NPs were carried out with inductively coupled plasma optical emission spectrometry (ICP-OES) on a SPECTRO GENESIS ICP spectrometer. TEM images were obtained using a JEOL 1400 (120 kV).

Ex situ x-ray absorption measurements was carried out at beamline 6.3.1.2 of the Advanced Light Source. PFY signal was collected via a Vortex silicon drift detector (SDD). TEY signal was measured as the drain current from the sample via an SRS 570 amplifier. All spectra were normalized by photon flux, represented by the TEY current measured from a gold mesh in the x-ray pipeline.

Acknowledgements

Author Contributions

The project was conceived by C.H.W. and C.L. under the supervision of S.Z, M.B.S. and C.B.M. Catalyst synthesis, basic characterization, and catalytic activity measurements were performed by C.L. and S.Z. AP-XPS experiments were conducted by C.H.W., H.T.F., and B.E. *Ex situ* TEM and elemental mapping were done by D.S. *In situ* TEM and EELS measurements were performed by H.X. *Ex situ* XAS measurements were done by C.H.W. The analysis and interpretation of all spectra (XPS, XAS, and EELS) were done by C.H.W. All author contributed to the writing of the manuscript.

Competing Financial Interests

The authors declare no competing financial interest.

References:

1. Dyakonov, A. & Robinson, E. Low-Temperature Oxidation of CO in Smoke: A Review. *Beiträge zur Tab. Int. to Tob. Res.* **22,** 88–106 (2006).

2. van Spronsen, M. A., Frenken, J. W. M. & Groot, I. M. N. Surface science under reaction conditions: CO oxidation on Pt and Pd model catalysts. *Chem. Soc. Rev.* **46,** 4347–4374 (2017).

3. Imbihl, R. Oscillatory reactions on single crystal surfaces. *Prog. Surf. Sci.* **44,** 185–343 (1993).

4. Rodriguez, J. a & Goodman, D. W. High-Pressure Catalytic Reactions over Single-Crystal Metal-Surfaces. *Surf. Sci. Rep.* **14,** 1–107 (1991).

5. Freund, H. J., Meijer, G., Scheffler, M., Schlögl, R. & Wolf, M. CO oxidation as a prototypical reaction for heterogeneous processes. *Angew. Chemie - Int. Ed.* **50,** 10064–10094 (2011).

6. Heck, R. M. & Farrauto, R. J. Automobile exhaust catalysts. *Appl. Catal. A Gen.* **221,** 443–457 (2001).

7. Twigg, M. V. Progress and future challenges in controlling automotive exhaust gas emissions. *Appl. Catal. B Environ.* **70,** 2–15 (2007).

8. Nilekar, A. U., Alayoglu, S., Eichhorn, B. & Mavrikakis, M. Preferential CO Oxidation in Hydrogen: Reactivity of Core-Shell Nanoparticles. *J. Am. Chem. Soc.* **132,** 7418–7428 (2010).

9. Fu, Q. *et al.* Interface-Confined Ferrous Centers for Catalytic Oxidation. *Science* **328,** 1141–1144 (2010).

10. Saavedra, J., Doan, H. a., Pursell, C. J., Grabow, L. C. & Chandler, B. D. The critical role of water at the gold-titania interface in catalytic CO oxidation. *Science* **345,** 1599–1602 (2014).

11. Wang, Y. G., Yoon, Y., Glezakou, V. A., Li, J. & Rousseau, R. The role of reducible oxide-metal cluster charge transfer in catalytic processes: New insights on the catalytic mechanism of CO oxidation on Au/TiO_2 from ab initio molecular dynamics. *J. Am. Chem. Soc.* **135,** 10673–10683 (2013).

12. Kim, H. Y., Lee, H. M. & Henkelman, G. CO Oxidation Mechanism on CeO_2-Supported Au Nanoparticles. *J. Am. Chem. Soc.* **134,** 1560–1570 (2012).

13. Widmann, D. & Behm, R. J. Active Oxygen on a Au/TiO2 Catalyst: Formation, Stability, and CO Oxidation Activity. *Angew. Chemie Int. Ed.* **50,** 10241–10245 (2011).

14. Haruta, M., Kobayashi, T., Sano, H. & Yamada, N. Novel Gold Catalysts for the Oxidation of Carbon Monoxide at a Temperature far Below 0 °C. *Chem. Lett.* **16,** 405–408 (1987).

15. Wang, C., Yin, H., Dai, S. & Sun, S. A General Approach to Noble Metal−Metal Oxide Dumbbell Nanoparticles and Their Catalytic Application for CO Oxidation. *Chem. Mater.* **22,** 3277–3282 (2010).

16. An, K. *et al.* Enhanced CO oxidation rates at the interface of mesoporous oxides and Pt nanoparticles. *J. Am. Chem. Soc.* **135,** 16689–16696 (2013).

17. Cargnello, M. *et al.* Control of Metal Nanocrystal Size Reveals Metal-Support Interface Role for Ceria Catalysts. *Science* **341,** 771–773 (2013).

18. Zhu, H. *et al.* Constructing Hierarchical Interfaces: TiO_2-Supported PtFe–FeO_x Nanowires for

Room Temperature CO Oxidation. *J. Am. Chem. Soc.* **137,** 10156–10159 (2015).

19.   Chen, G. *et al.* Interfacial Effects in Iron-Nickel Hydroxide-Platinum Nanoparticles Enhance Catalytic Oxidation. *Science* **344,** 495–499 (2014).

20.   Shan, S. *et al.* Atomic-Structural Synergy for Catalytic CO Oxidation over Palladium-Nickel Nanoalloys. *J. Am. Chem. Soc.* **136,** 7140–51 (2014).

21.   Zhan, W. *et al.* Crystal Structural Effect of AuCu Alloy Nanoparticles on Catalytic CO Oxidation. *J. Am. Chem. Soc.* **139,** 8846–8854 (2017).

22.   Gilroy, K. D., Ruditskiy, A., Peng, H.-C., Qin, D. & Xia, Y. Bimetallic Nanocrystals: Syntheses, Properties, and Applications. *Chem. Rev.* **116,** 10414–10472 (2016).

23.   Yu, W., Porosoff, M. D. & Chen, J. G. Review of Pt-Based Bimetallic Catalysis: From Model Surfaces to Supported Catalysts. *Chem. Rev.* **112,** 5780–5817 (2012).

24.   Guo, S., Zhang, S. & Sun, S. Tuning Nanoparticle Catalysis for the Oxygen Reduction Reaction. *Angew. Chemie Int. Ed.* **52,** 8526–8544 (2013).

25.   Tao, F. *et al.* Reaction-driven restructuring of Rh-Pd and Pt-Pd core-shell nanoparticles. *Science* **322,** 932–4 (2008).

26.   Tao, F. *et al.* Evolution of structure and chemistry of bimetallic nanoparticle catalysts under reaction conditions. *J. Am. Chem. Soc.* **132,** 8697–703 (2010).

27.   Carenco, S. *et al.* Dealloying of Cobalt from CuCo Nanoparticles under Syngas Exposure. *J. Phys. Chem. C* **117,** 6259–6266 (2013).

28.   Ogletree, D. F. *et al.* A differentially pumped electrostatic lens system for photoemission studies in the millibar range. *Rev. Sci. Instrum.* **73,** 3872 (2002).

29.   Wu, C. H., Weatherup, R. S. & Salmeron, M. B. Probing electrode/electrolyte interfaces in situ by X-ray spectroscopies: old methods, new tricks. *Phys. Chem. Chem. Phys.* **17,** 30229–30239 (2015).

30.   Zheng, H., Meng, Y. S. & Zhu, Y. Frontiers of in situ electron microscopy. *MRS Bull.* **40,** 12–18 (2015).

31.   Escudero, C. *et al.* A reaction cell with sample laser heating for in situ soft X-ray absorption spectroscopy studies under environmental conditions. *J. Synchrotron Radiat.* **20,** 504–508 (2013).

32.   Heine, C. *et al.* Ambient-pressure soft X-ray absorption spectroscopy of a catalyst surface in action: Closing the pressure gap in the selective n-butane oxidation over vanadyl pyrophosphate. *J. Phys. Chem. C* **118,** 20405–20412 (2014).

33.   Bluhm, H., Ogletree, D. F., Fadley, C. S., Hussain, Z. & Salmeron, M. The premelting of ice studied with photoelectron spectroscopy. *J. Phys. Condens. Matter* **14,** L227–L233 (2002).

34.   Sun, D., Mazumder, V., Metin, O. & Sun, S. Catalytic Hydrolysis of Ammonia Borane via Cobalt Palladium Nanoparticles. *ACS Nano* **5,** 6458–6464 (2011).

35.   Sun, S. & Murray, C. B. Synthesis of monodisperse cobalt nanocrystals and their assembly into magnetic superlattices (invited). *J. Appl. Phys.* **85,** 4325–4330 (1999).

36.   Zhang, S. *et al.* Monodisperse Core/Shell Ni/FePt Nanoparticles and Their Conversion to Ni/Pt to Catalyze Oxygen Reduction. *J. Am. Chem. Soc.* **136,** 15921–15924 (2014).

37. Ishida, K. & Nishizawa, T. The C-Co (Carbon-Cobalt) System. *J. Phase Equilibria* **12,** 417–424 (1991).

38. Toyoshima, R. *et al.* Active surface oxygen for catalytic CO oxidation on Pd(100) proceeding under near ambient pressure conditions. *J. Phys. Chem. Lett.* **3,** 3182–3187 (2012).

39. Ketteler, G. *et al.* In situ spectroscopic study of the oxidation and reduction of Pd(111). *J. Am. Chem. Soc.* **127,** 18269–73 (2005).

40. Gries, W. H. Angular intensity modulation in angle-resolved XPC and AES of non-crystalline ultrathin surface layers: The phenomenon and its implications. *Surf. Interface Anal.* **17,** 803–812 (1991).

41. Kibis, L. S., Titkov, A. I., Stadnichenko, A. I., Koscheev, S. V. & Boronin, A. I. X-ray photoelectron spectroscopy study of Pd oxidation by RF discharge in oxygen. *Appl. Surf. Sci.* **255,** 9248–9254 (2009).

42. Militello, M. C. Palladium Oxide (PdO) by XPS. *Surf. Sci. Spectra* **3,** 395 (1994).

43. Balmes, O. *et al.* Reversible formation of a PdCx phase in Pd nanoparticles upon CO and O2 exposure. *Phys. Chem. Chem. Phys.* **14,** 4796 (2012).

44. Rogal, J., Reuter, K. & Scheffler, M. CO oxidation at Pd(100): A first-principles constrained thermodynamics study. *Phys. Rev. B - Condens. Matter Mater. Phys.* **75,** 1–11 (2007).

45. Wu, C. H., Eren, B., Bluhm, H. & Salmeron, M. B. Ambient-Pressure X-ray Photoelectron Spectroscopy Study of Cobalt Foil Model Catalyst under CO, H$_2$, and Their Mixtures. *ACS Catal.* 1150–1157 (2017). doi:10.1021/acscatal.6b02835

46. Wang, Z. L., Bentley, J. & Evans, N. D. Valence state mapping of cobalt and manganese using near-edge fine structures. *Micron* **31,** 355–362 (2000).

47. Wang, Z. L., Yin, J. S. & Jiang, Y. D. EELS analysis of cation valence states and oxygen vacancies in magnetic oxides. *Micron* **31,** 571–580 (2000).

48. Lee, A. F. & Lambert, R. M. Oxidation of Sn overlayers and the structure and stability of Sn oxide films on Pd(111). *Phys. Rev. B - Condens. Matter Mater. Phys.* **58,** 4156–4165 (1998).

49. Batzill, M., Beck, D. E., Jerdev, D. & Koel, B. E. Tin-oxide overlayer formation by oxidation of Pt–Sn(111) surface alloys. *J. Vac. Sci. Technol. A Vacuum, Surfaces, Film.* **19,** 1953 (2001)
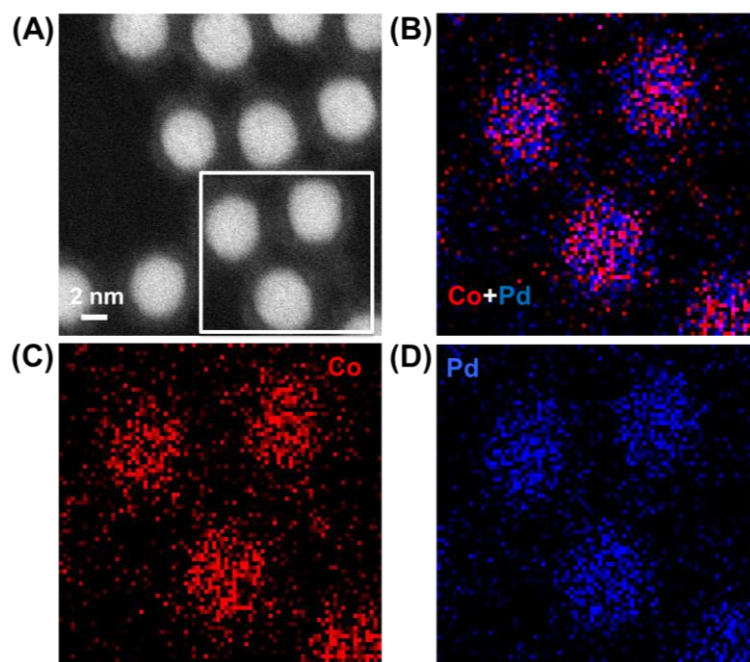
Figure 2. STEM and EELS elemental mapping of 4.5nm as-synthesized $Co_{0.26}Pd_{0.74}$ NPs. (A), Representative dark-field STEM image of $Co_{0.26}Pd_{0.74}$ NPs. Overlaid Co+Pd (B), Co (C), and Pd (D) EELS mapping of the four NPs within the white frames marked in (A).
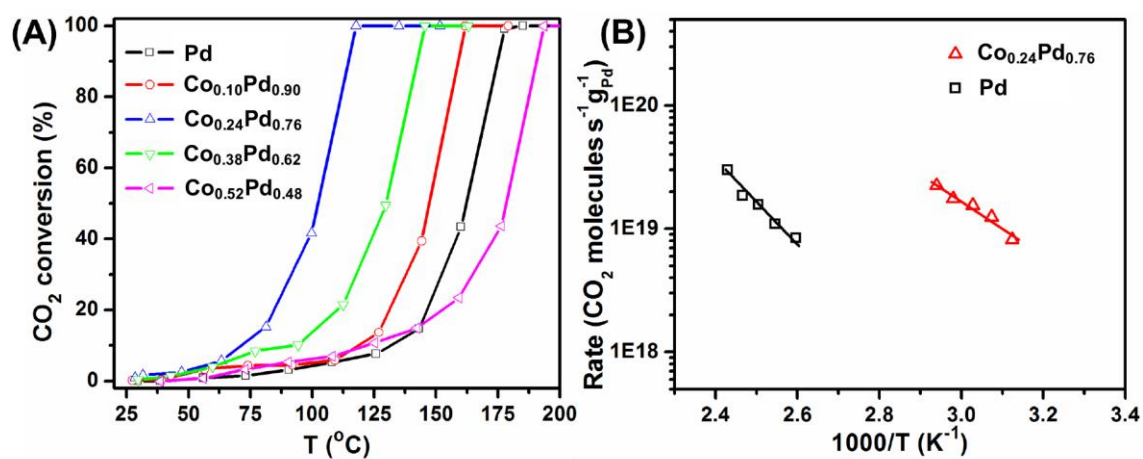

Figure 1. Catalytic performance of Pd and CoPd NPs. (A), Light-off curves of Pd NPs and four CoPd alloy NPs in CO oxidation reactions. (B), Arrhenius plot of $Co_{0.26}Pd_{0.74}$ and Pd NPs.
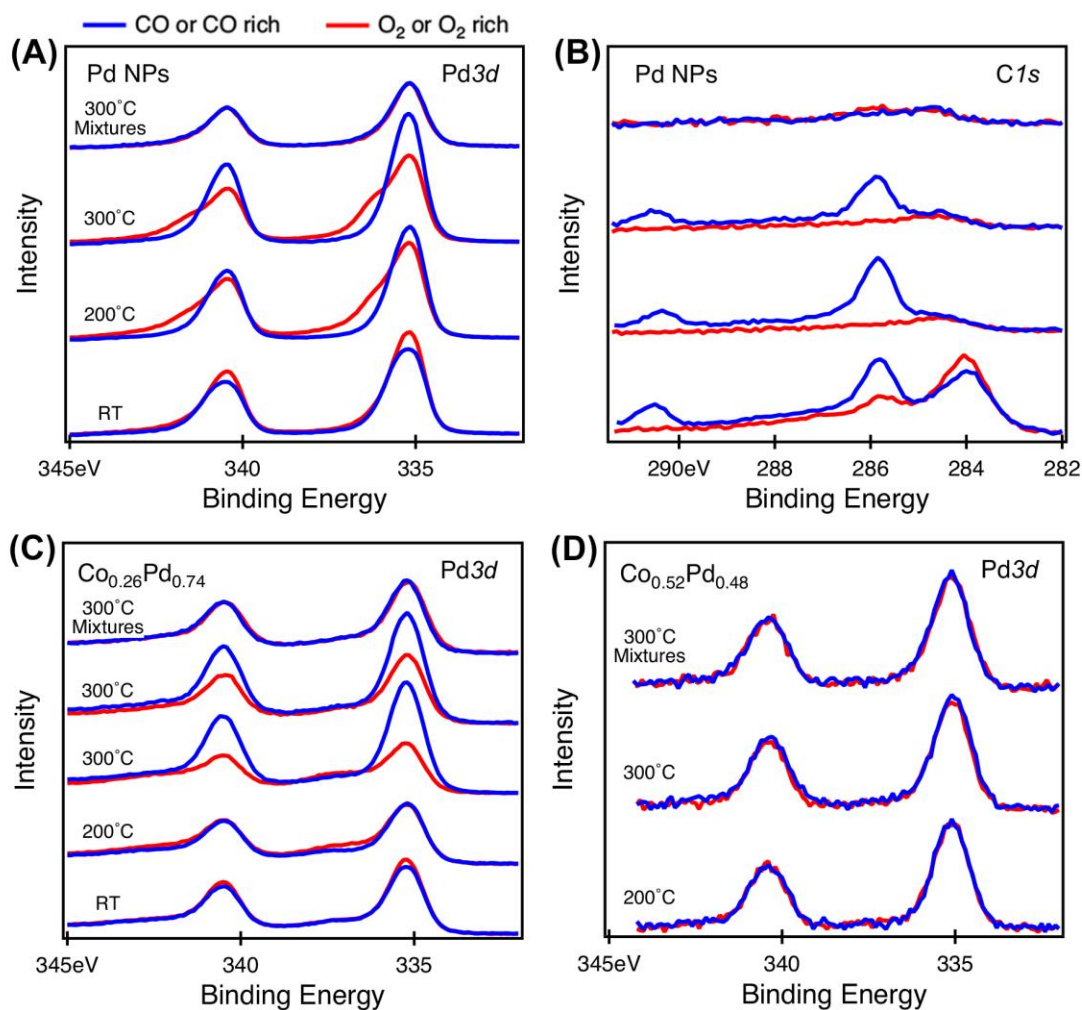
Figure 3. AP-XPS measurements on Pd and PdCo NPs under reaction conditions. Evolution of Pd*3d* (A) and C*1s* (B) spectra for Pd NPs, Pd*3d* spectra for $Pd_{0.26}Co_{0.74}$ (C) NPs, and Pd*3d* spectra for $Co_{0.52}Pd_{0.48}$ NPs (D) under 100mTorr of CO, O_2, and their mixtures at different temperatures. Blue spectra were acquired under CO only or CO rich (4 CO : 1 O_2) conditions; Red spectra were acquired under O_2 only or O_2 rich (1 CO : 4 O_2) conditions.
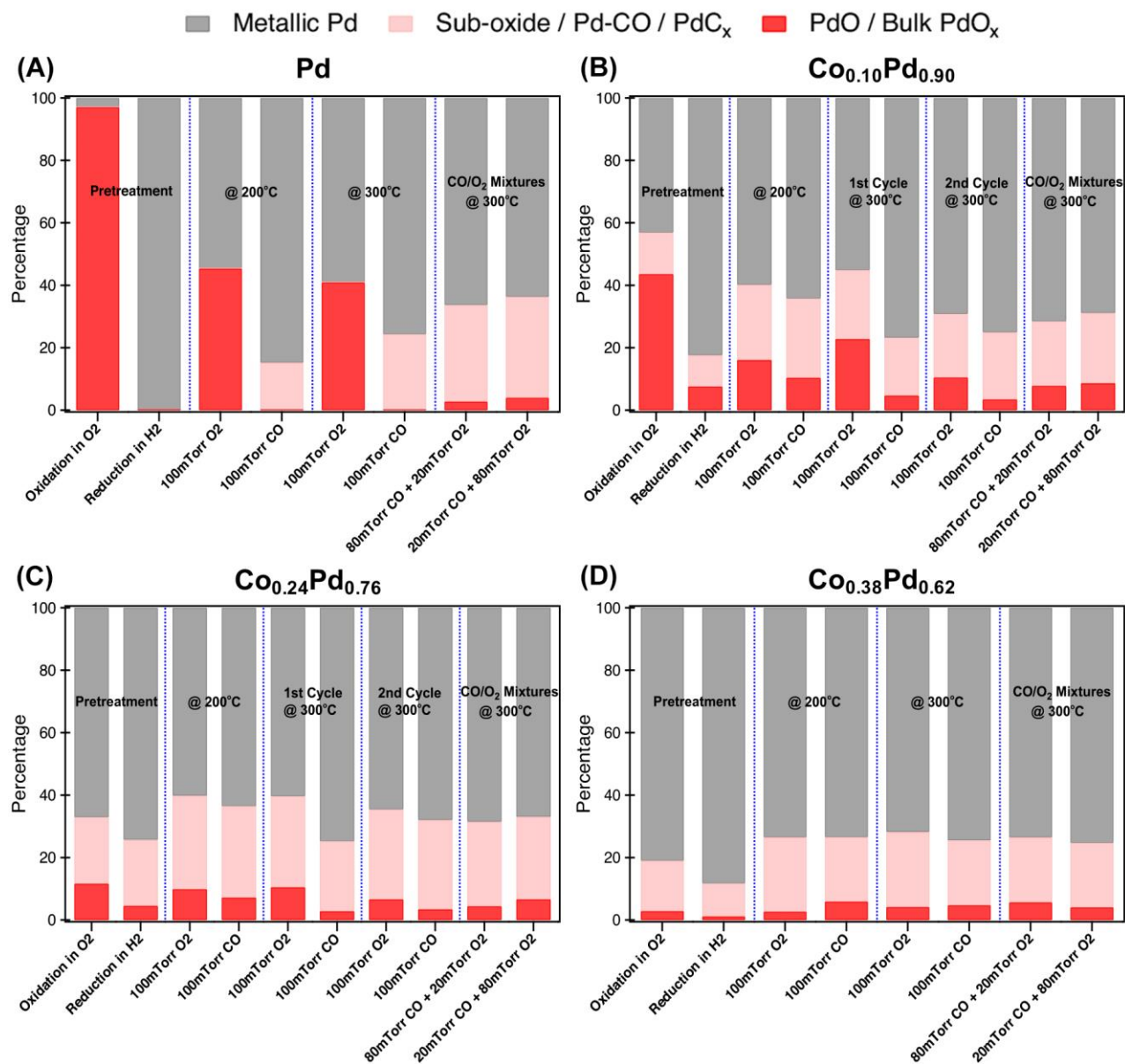
Figure 4. Surface Pd speciation for Pd (A), $Co_{0.10}Pd_{0.90}$ (B), $Co_{0.26}Pd_{0.74}$ (C), and $Co_{0.38}Pd_{0.62}$ NPs (D) under different conditions, based on peak deconvolution of Pd$3d$ spectra.
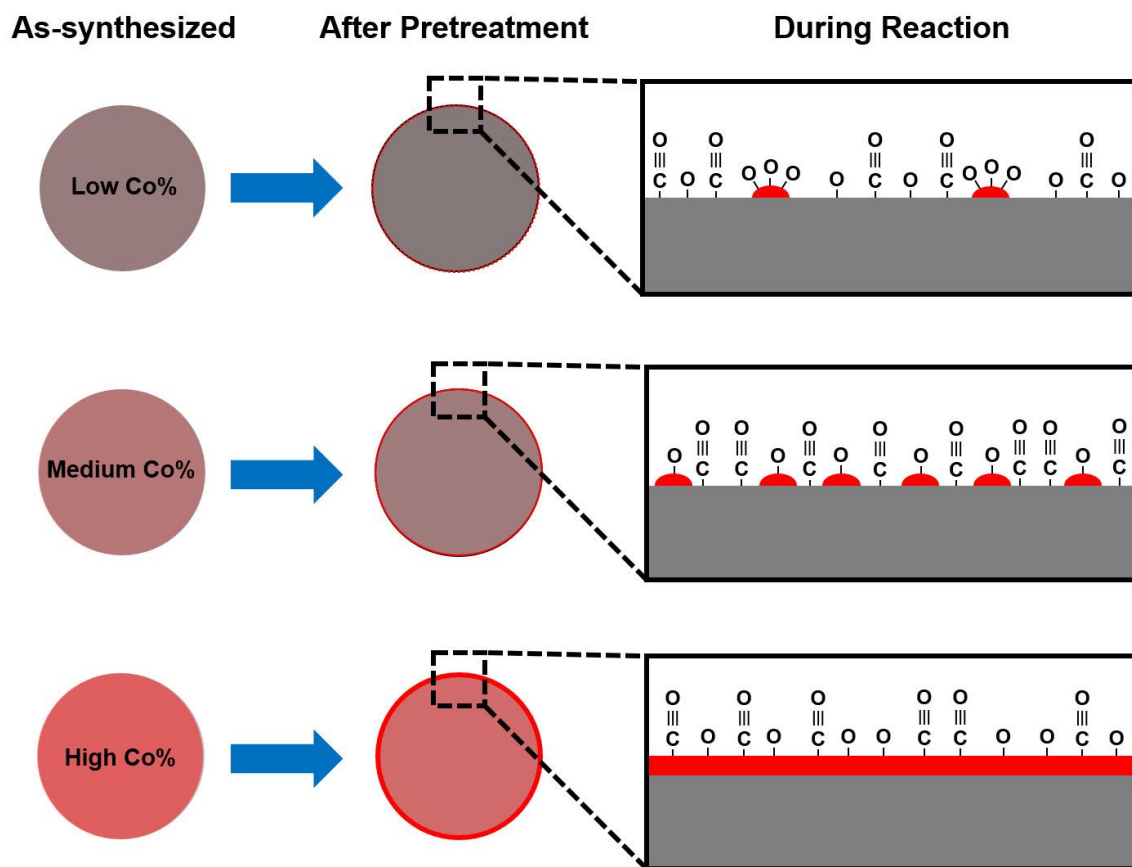
Figure 5. Schematic illustration of the surface evolution and proposed bimetallic synergy in CoPd alloy NPs with low, medium and high Co content.
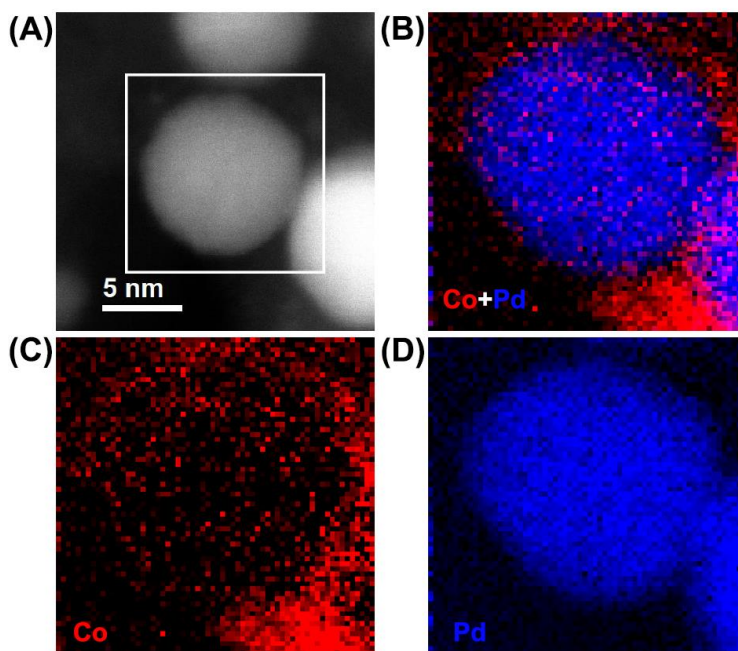
Figure 6. STEM and EELS elemental mapping of 10nm $Co_{0.26}Pd_{0.74}$ NPs after pretreatment. (A), Representative dark-field STEM image of $Co_{0.26}Pd_{0.74}$ NPs. Overlaid Co+Pd (B), Co (C), and Pd (D) EELS mapping of the four NPs within the white frames marked in (A).
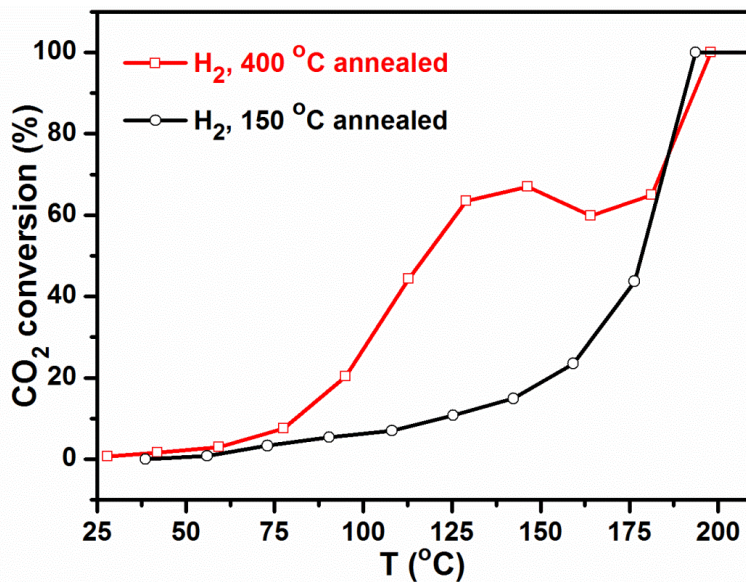
Figure 6. CO oxidation light-off curves of $Co_{0.52}Pd_{0.48}$ NPs that underwent H_2 pretreatment at 150°C and 400°C.

Supplementary Information

A. Process and analysis procedures of XPS, EELS, XAS spectra

A1. XPS spectra

The energy scales of all XPS spectra were calibrated by shifting the Fermi edge positions measured with corresponding photon energy to zero. The Pd$3d$ spectra of $Co_{0.38}Pd_{0.62}$ and $Co_{0.52}Pd_{0.48}$ have a rather surprising shift of 0.4-0.5 eV towards lower binding energy as well as drastically different fermi edge line shape, which we cannot fully understand or explain. Because all the elements went through certain chemical changes during the experiments, including Si in the substrate, it is difficult to use the peak of any particular elements as internal calibration reference. Tentatively, we aligned the main peak in Pd$3d$ spectra for these two samples with the other three samples. Given the fact that these two samples barely showed changes in the surface composition, such realignment does not affect the validity of our conclusion. Because of slightly different attenuation of 100mTorr and 100mTorr O_2, for the purpose of better visual comparison, in the figures where spectra under oxidation/reduction conditions were overlaid, the spectra were normalized at the lower energy end of the spectra.

Pd$3d$ XPS spectra were quantitatively analyzed by peak deconvolution using casaXPS software, preceded by subtracting a Shirley-type background. The metallic Pd component was fitted using an asymmetric line shape DS(0.01,175)SGL(30), which was determined by optimizing the fitting results on the fully reduced pure Pd NPs after treated in H_2 at 150°C. The components related to rest of the Pd species, including surface sub-xoide, CO-coordinated Pd, surface PdC_x, and bulk PdO_x, were fitted using line shapes of symmetric SGL functions. Peak fitting was not performed the Pd$3d$ spectra of $Co_{0.52}Pd_{0.48}$ NPs because of their low signal-to-noise ratios and relatively unchanged shapes during the entire experiments.

Co$3p$/Pd$4p$ spectra was used to estimate the surface Co/Pd ratios. The information depth of these spectra is estimated to ~0.9 nm according to NIST Electron Inelastic-Mean-Free-Path Database (Version 1.2).

In-depth analysis of Co oxidation states as well as accurate calculation of the Co/Pd ratios is impossible for multiple reasons, including substantial overlapping of Pd*4p* high energy tails under Co*3p* main peak, the spin-orbital splitting of both elements that cannot be well resolved, as well as the coexistence of multiple Co and Pd species. A crude fitting procedure was performed for the sole purpose of estimating the peak areas, as illustrated in Figure S7, preceded by subtracting a linear background, except for $Co_{0.38}Pd_{0.62}$, in which case a Shirley-type background is necessary to avoid negative peak intensity. The Co/Pd ratios were then calculated from the peak areas (PA) of Co*3p* and Pd*4p* signals, ionization cross sections (ICS) of each element at the corresponding incident photon energies, using the following formula:

$$Atomic\ Ratio\ \frac{Co}{Pd} = \frac{PA(Co)}{PA(Pd)} \times \frac{ICS(Pd)@500eV}{ICS(Co)@500eV}$$

A2. EELS spectra

Raw EELS spectra acquired from ETEM/EELS experiments were processed using the open-source Cornell Spectrum Imager following the method described in the article by R. Hovden et al. (*Microscopy Today 2013, 21, 40-44*). A power function was used for background subtraction and each spectrum was then normalized by L_3 peak intensity. All spectra in Figure S9a were shifted to align the L_3 peak to ~778eV. The areas of L_3 and L_2 peaks were calculated by integrating the spectra under L_3 peak (770eV, 786eV) and under L_2 peak (788eV, 802eV) respectively, preceded by subtracting a linear background within each energy window.

A3. XAS spectra

The energy scales of all Co L-edge XAS spectra were calibrated by first shifting the L_3 peak of a Co metal foil reference sample to 778.1 eV and then applying the same energy shift to all the subsequently

acquired Co L-edge spectra. All XAS spectra were first normalized by the photon flux profile represented by a TEY current collected on a gold mesh in the upstream x-ray pipeline. After a linear background was subtracted from each spectrum based on the slope of the pre-edge region, the spectra were normalized again by setting L_3 peak intensity to 1.

B. Thickness estimation of CoO_x shell for a $Co_{0.25}Pd_{0.75}$ particle

A back-of-the-envelope calculation of Co shell thickness might help us understand why it is difficult to image these thin Co shells. Assuming all of the Co atoms in the $Co_{0.25}Pd_{0.75}$ particles redistribute uniformly to the surface of 4.5nm sphere (ignore the density difference between Co and Pd) and form a thin shell with thickness of Δr. The percentage of Co can be expressed in the following equation:

$$Co\% = 1 - \frac{Volume\ of\ Pd\ core}{Volume\ of\ entire\ particle} = 1 - \frac{(4.5 - \Delta r)^3}{4.5^3} = 0.25.$$

Solve this equation and we get $\Delta r \sim 0.4$nm. If all the Co were oxidized to CoO (~40% volume expansion), the CoO_x shell will be less than 0.6nm, about two atomic layers, which will be very challenging to image, even more so in the case of lower Co-content particles and/or under in-situ conditions.

For a larger particle (e.g. 10nm diameter) with the same Co content, solve the same equation and we get $\Delta r \sim 0.9$nm. We can expect a ~1.3nm oxide shell after oxidation, which should be much easier to observe in STEM.

If we assume the thickness of a perfect monolayer is ~ 0.3nm, we can also estimate the overall Co percentage in a 4.5nm CoPd particle where the Pd core is covered by a perfect monolayer of Co:

$$Co\% = 1 - \frac{(4.5 - 0.3)^3}{4.5^3} = 19\%$$

C. Supporting Figures: Figure S1 - S12
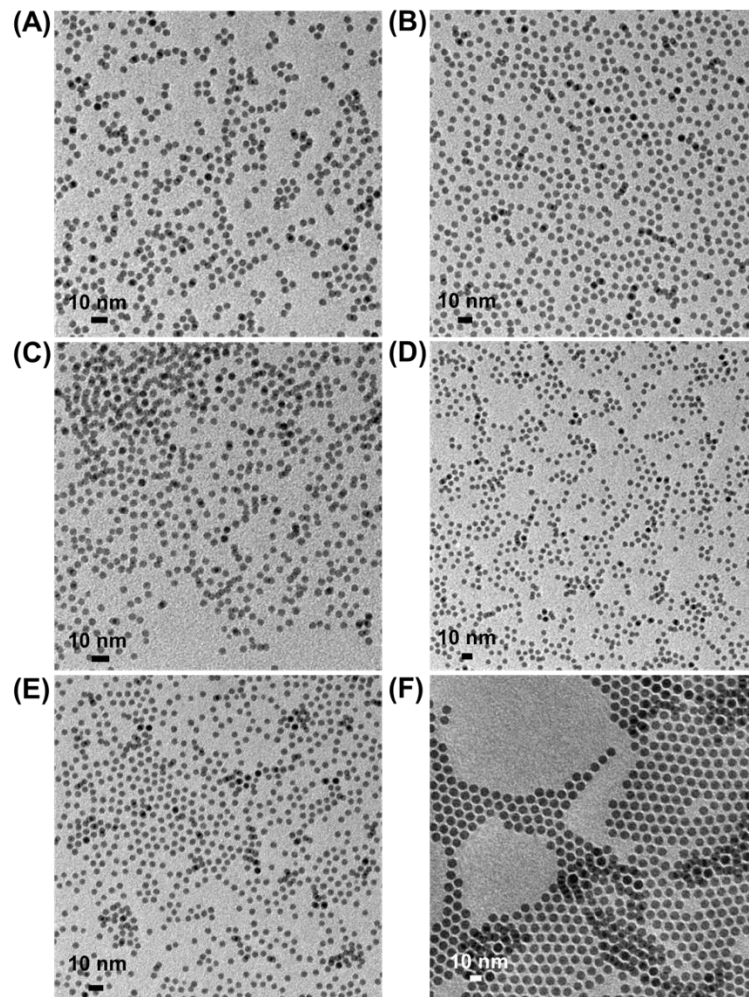
Figure S1. (**A-E**) TEM image of as-synthesized $Co_{0.10}Pd_{0.90}$ (**A**), $Co_{0.26}Pd_{0.74}$ (**B**), $Co_{0.38}Pd_{0.62}$ (**C**), $Co_{0.52}Pd_{0.48}$ (**D**) and Pd (**E**) NPs in the presence of TBP. (**F**) TEM image of as-synthesized $Co_{0.26}Pd_{0.74}$ NPs in the presence of TOP.
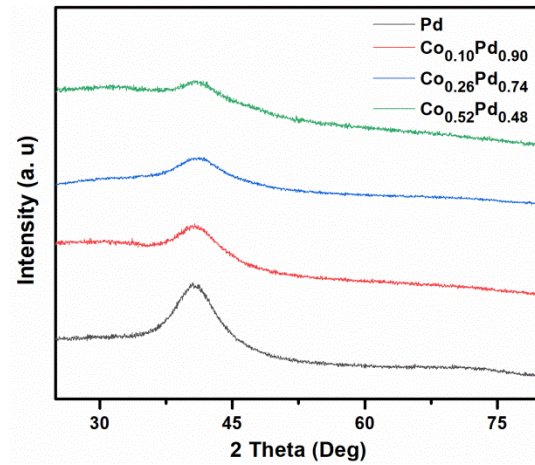
Figure S2. XRD patterns of as-synthesized Pd, $Co_{0.10}Pd_{0.90}$, $Co_{0.26}Pd_{0.74}$ and $Co_{0.52}Pd_{0.48}$ NPs.
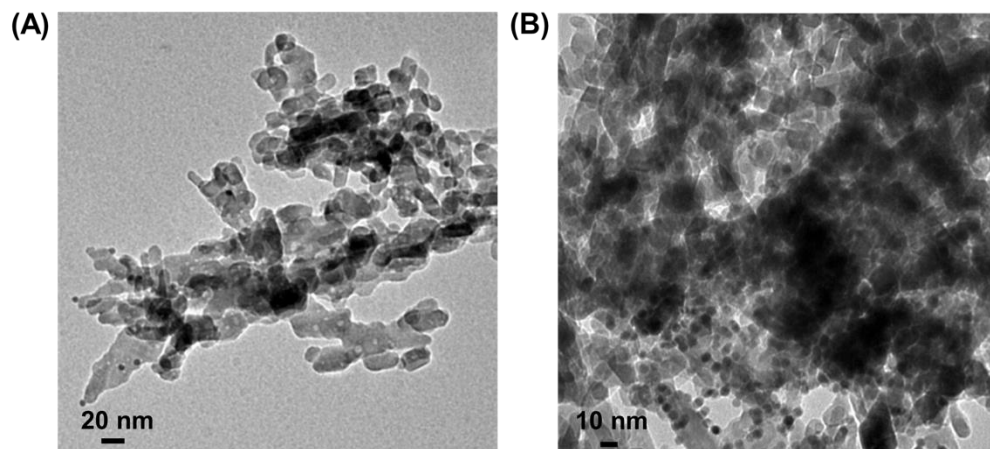
Figure S3. TEM image of $Co_{0.26}Pd_{0.74}$ NPs supported on Al_2O_3 before (A) and after (B) pre-treatment (annealed in air at 300 °C for 3 hours).
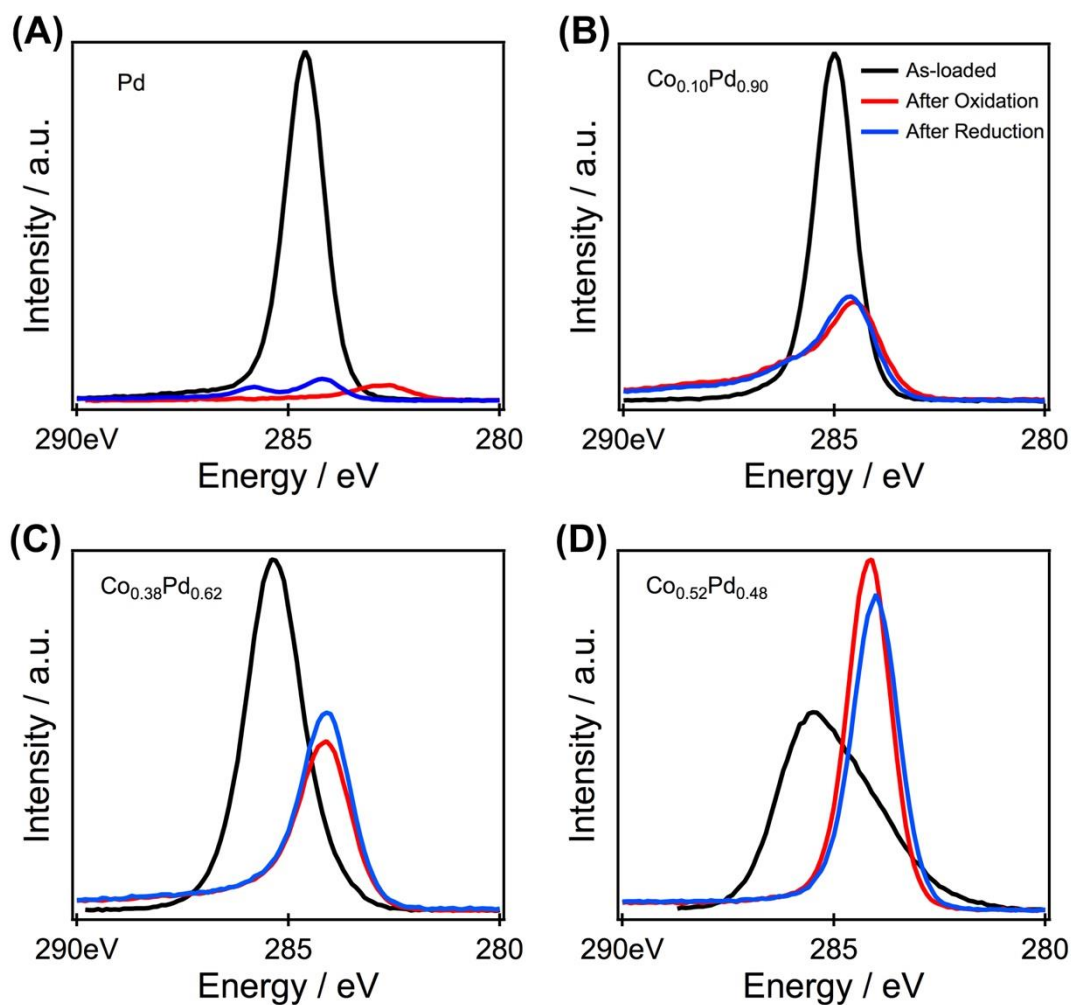
Figure S4. C*1s* spectra of (A) Pd, (B) $Co_{0.10}Pd_{0.90}$, (C) $Co_{0.38}Pd_{0.62}$, and (D) $Co_{0.52}Pd_{0.48}$ before and after pre-treatments.
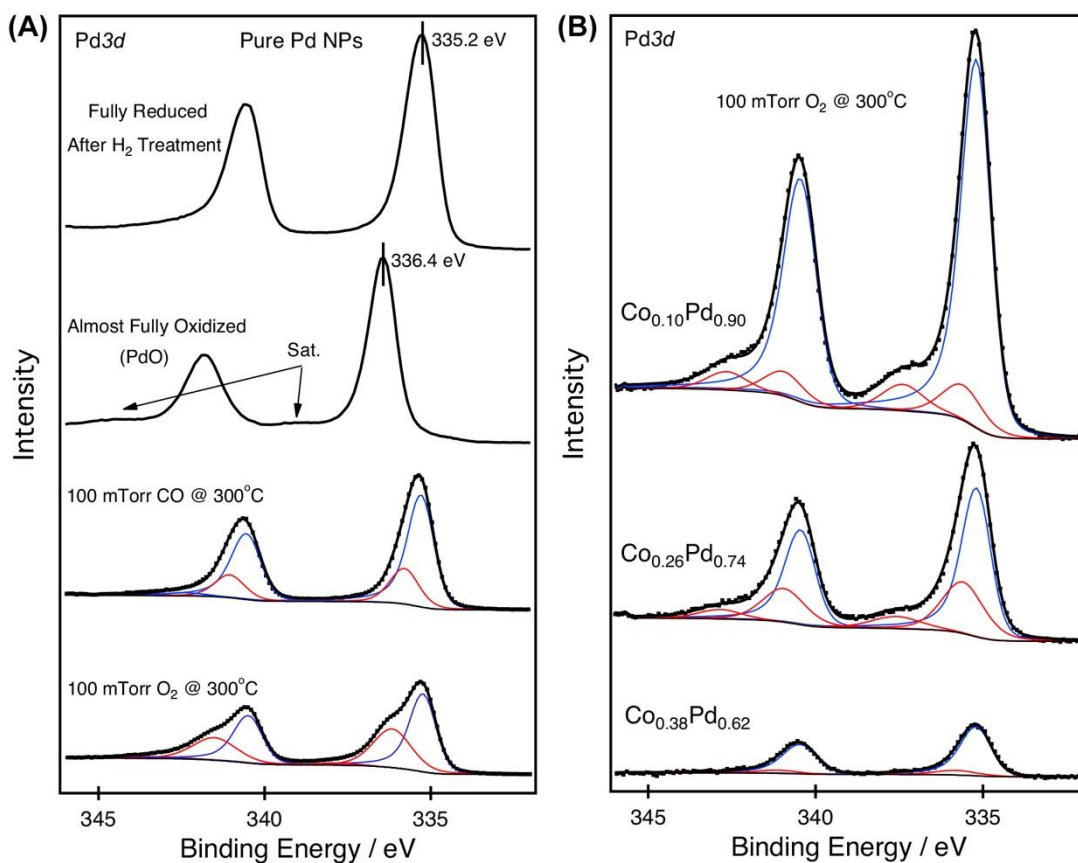
Figure S5. (A) Pd*3d* spectra of Pd NPs when fully reduced (in H_2) and fully oxidized (in O_2) Pd NPs during the pre-treatments, and deconvoluted Pd*3d* spectra when Pd NPs were exposed to 100 mTorr of CO or O_2 at 300°C. (B) Deconvoluted Pd*3d* spectra of $Co_{0.10}Pd_{0.90}$, $Co_{0.26}Pd_{0.74}$, and $Co_{0.38}Pd_{0.62}$ under 100 mTorr of O_2 at 300°C. Blue components represent metallic Pd; Red components represent oxidized Pd species.
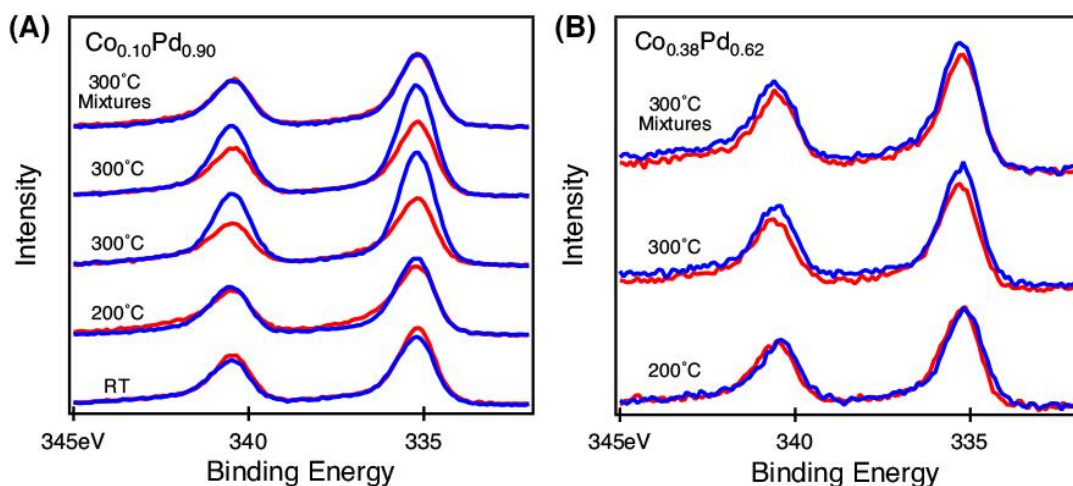
Figure S6. Pd$3d$ spectra of (A) $Co_{0.10}Pd_{0.90}$ and (B) $Co_{0.38}Pd_{0.62}$ NPs under 100mTorr of CO, O_2, and their mixtures (1:4 or 4:1) at different temperatures. Blue spectra were acquired under CO only or CO rich conditions; Red spectra were acquired under O_2 only or O_2 rich conditions.
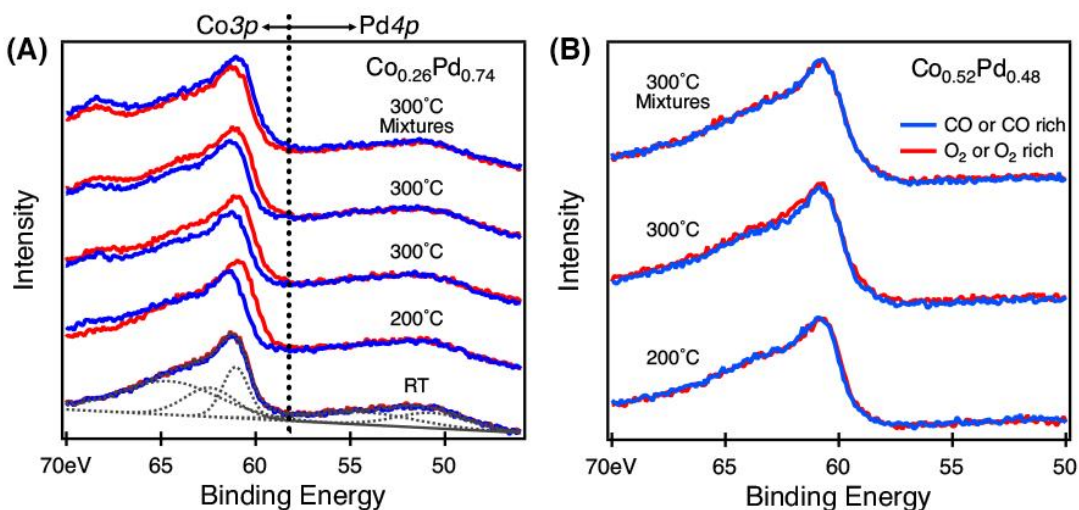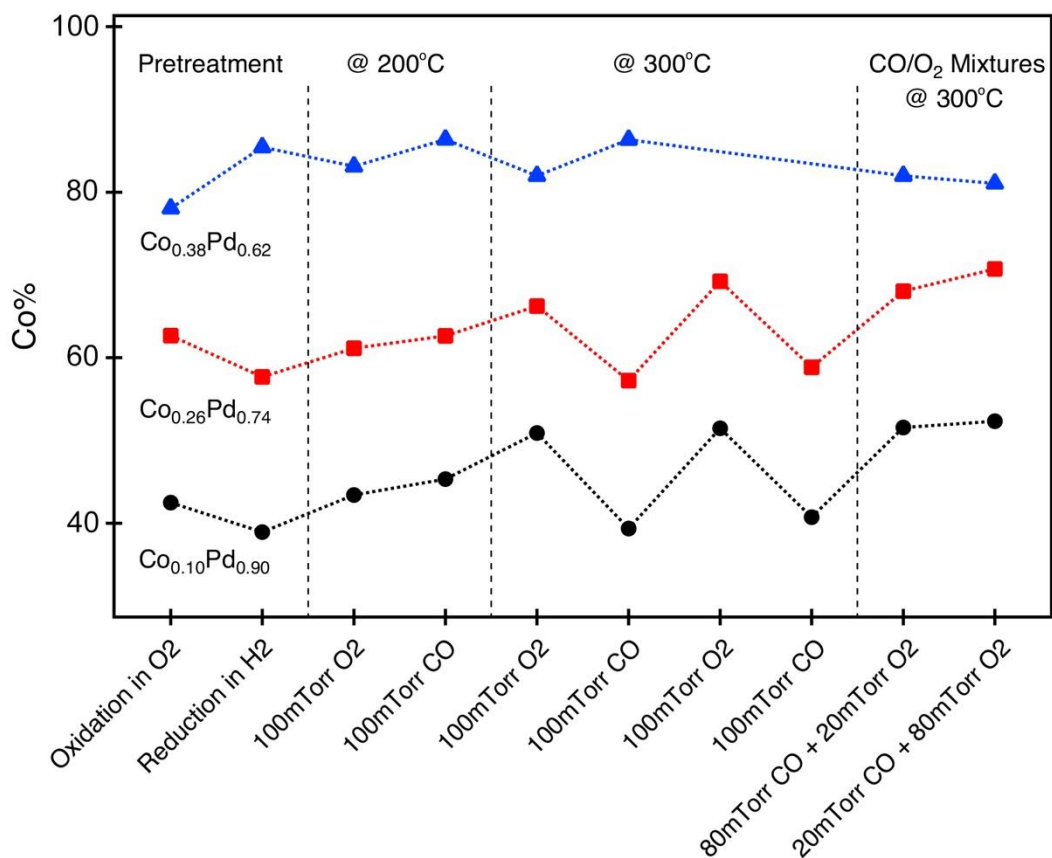
Figure S7. Co$3p$/Pd$4p$ spectra of (A) Co$_{0.26}$Pd$_{0.74}$ and (B) Co$_{0.52}$Pd$_{0.48}$ NPs under 100mTorr of CO, O$_2$, and their mixtures (1:4 or 4:1) at different temperatures. Blue spectra were acquired under CO only or CO rich conditions; Red spectra were acquired under O$_2$ only or O$_2$ rich conditions.

Figure S8. Percentage of Co (metal basis) under different conditions, estimated from the peak area ratios in Co$3p$/Pd$4p$ spectra for Co$_{0.10}$Pd$_{0.90}$, Co$_{0.26}$Pd$_{0.74}$, and Co$_{0.38}$Pd$_{0.62}$ NPs.
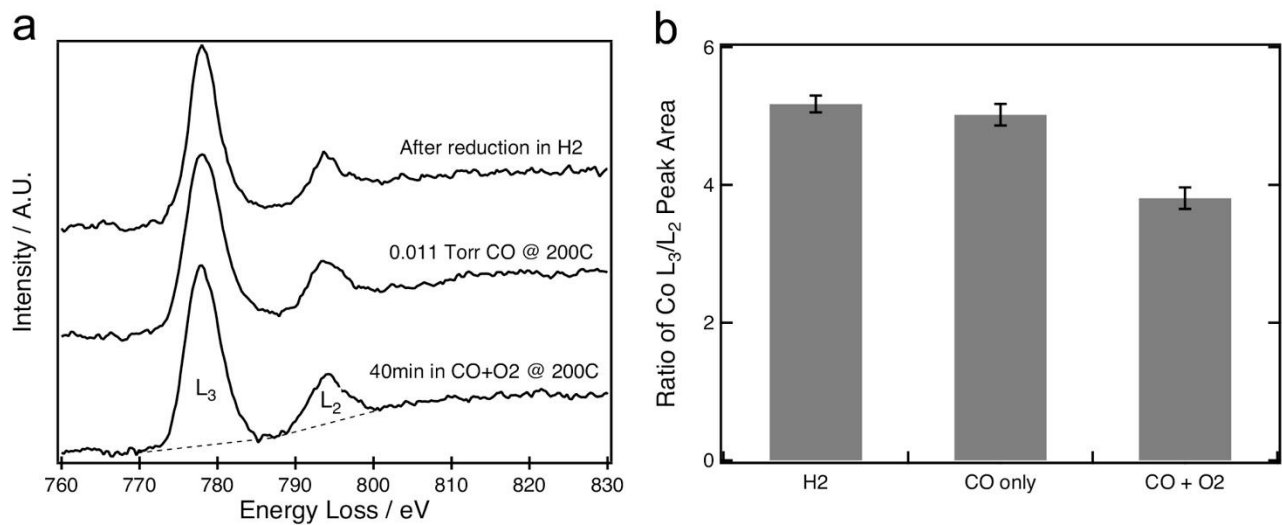
Figure S9. (a) Co L-edge EELS spectra acquired after reduction in H_2, while heating in 0.11 Torr CO at 200°C, and after 40min heating in 0.11 Torr CO and 0.44 Torr O_2 at 200°C. (b) Corresponding L_3/L_2 ratios under three different conditions.
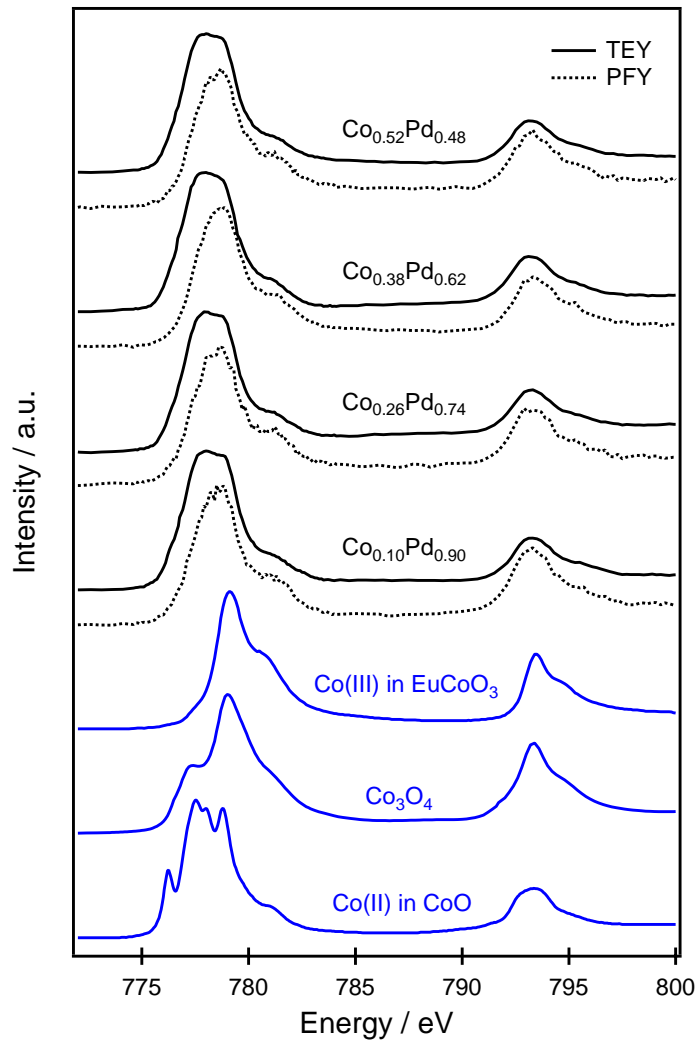
Figure S10. *Ex-situ* Co L-edge XAS TEY (solid) and PFY (dotted) spectra of CoPd alloy NPs after APXPS measurements, in comparison with reference spectra of different Co compounds.
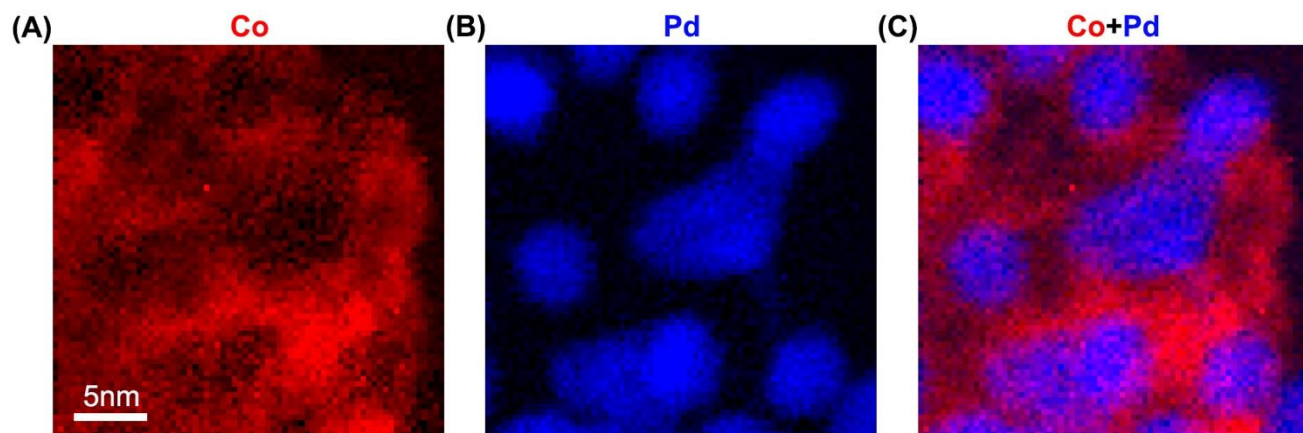
Figure S11. Representative STEM-EELS elemental mapping of Co (A), Pd (B), and overlaid Co+Pd (C) of $Co_{0.52}Pd_{0.48}$ NPs (supported on carbon) after pre-treatment.
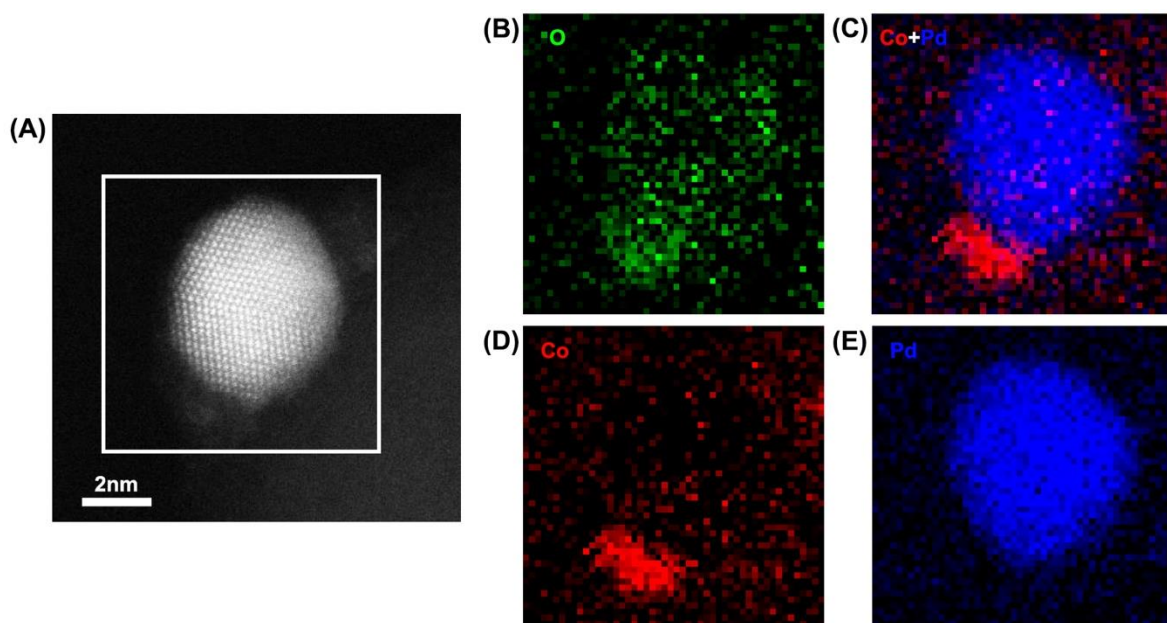

Figure S12. STEM and EELS elemental mapping of pre-treated 4.5nm $Co_{0.26}Pd_{0.74}$ NPs. (A), Representative dark-field STEM image of $Co_{0.26}Pd_{0.74}$ NPs. O (B), overlaid Co+Pd (C), Co (D), and Pd (E) EELS mapping of the NP.